Encoding Desired Deformation Profiles in Endoscope-Like Soft Robots

Daniel S. Esser, Margaret F. Rox, Robert P. Naftel, D. Caleb Rucker, Eric J. Barth, Alan Kuntz,
and Robert J. Webster III

***Abstract*—Prior models of continuously flexible robots typically assume uniform stiffness, and in this paper we relax this assumption. Geometrically varying stiffness profiles provide additional design freedom to influence the motions and workspaces of continuum robots. These results are timely, because with recent rapid advancements in multimaterial additive manufacturing techniques, it is now straightforward to create more complex stiffness profiles in robots. The key insight of this paper is to project forces and moments applied to the robot onto its center of stiffness (i.e. the Young's modulus-weighted center of each cross section). We show how the center of stiffness can be thought of as analogous to a "precurved backbone" in a robot with uniform stiffness. This analogy enables a large body of prior work in Cosserat Rod modeling of such robots to be applied directly to those with stiffness variations. We experimentally validate this approach using multimaterial, soft, tendon-actuated robots. Lastly, to illustrate how these results can be used in practice, we investigate how stiffness variation can improve performance in a neurosurgical task.**

INTRODUCTION

The flexible and curvilinear nature of continuum robots enables them to navigate through narrow, constrained environments where rigid robots are not sufficiently dexterous. These robots typically have an elastic backbone running down their centerline, or have distributed elasticity that can be modeled as such. They can be actuated by tendons that apply loads on the elastic body, causing them to deform in desired directions. The stiffness properties of the backbone dictate how the robot's shape responds to actuation or external loads. Such robots have been applied to surgical applications [1]–[4], industrial tasks [5]–[9], and even designed for use in outer space [10], [11], among other applications. In many such applications, the inherent compliance of these robots provides safety as they interact with their surrounding environment.

Some of the earliest examples of flexible robots consisted of hyperredundant snake-like robots with many rigid sections connected by passive elastic or actuated joints [12]–[14]. In contrast with hyperredundant robots, which have a finite number of unactuated degrees of freedom (DOF), continuum and soft robots, inspired by analogous tentacle arms found in biology [15], have an infinite number of DOF because they bend continuously. A variety of actuation approaches have been proposed for continuum robots, including pneumatics (see e.g. [16]), flexible push-pull rods [17], concentric tube robots [18], [19], and tendon actuation [20], [21].

Early continuum robots used simple actuators, such as straight tendons or pneumatic bellows and typically took on constant curvature shapes when actuated [22], [23]. More recently the effects of nonlinearly routed tendons have been modeled [24], increasing the design space for continuum robots (see e.g. [25], [26]). The stiffness properties of the backbone map loads into motions, and we believe that there is an opportunity to consider stiffness design in more detail to endow such robots with new properties.

In contrast with continuum robots, which typically have a central backbone along which they bend, soft robots are usually made entirely out of soft elastomers with no distinct backbone (see e.g. [15]). Soft robotic systems use variable material stiffness and geometry to mechanically encode desired deformations. Pneumatically-actuated soft robots are typically designed to have higher stiffness in certain directions to induce preferential modes of deformation, (see e.g. [27]–[31]), or to change how soft robots grip objects [32].

Prior work considering more general stiffness profiles in continuum robots has included an asymmetric stiffness pneumatic robot design proposed by [33], where the stiffness properties of the stiffer and softer segment were modeled as two offset springs, and their relative stiffness was used to tune the ratio of bending to elongation. Additional secondary backbones have been proposed to change the stiffness profile of a tendon-driven manipulator, to enable high-precision micromotions [34]. Barrientos-Diez et al. [35] used asymmetric joints to create segments of a TDCR manipulator that bend with constant curvature in preferential bending directions. Recently, concentric push-pull robots have been made from collections of laser patterned tubes whose stiffness centers are offset from each other [36], [37].

This paper builds on the interest in asymmetric stiffness profiles, presenting a rod-based modeling approach for continuum robots with asymmetric and inhomogeneous stiffness profiles. By conceptualizing the stiffness center as a (potentially) precurved symmetric beam, the robot's deformation can be directed in different ways by shifting the position of the stiffness center relative to the tendon, as illustrated in Fig. 2b.

Cosserat rod theory has also been used to model the

D. S. Esser, M. Rox, E. J. Barth, and R. J. Webster III are with the Department of Mechanical Engineering, Vanderbilt University, Nashville, TN 37212 USA

A. Kuntz is with the Robotics Center and the Kahlert School of Computing at the University of Utah, Salt Lake City, UT 84112, USA.

D. C. Rucker is with the Department of Mechanical Engineering, University of Tennessee Knoxville, USA

This material is based upon work supported in part by the National Science Foundation under grant numbers 2133027 and 1935278, the National Institutes of Health (NIH) under NIBIB training grant T32EB021937, and the Natural Sciences and Engineering Research Council of Canada (NSERC) under grant 521537544. Any opinions, findings, and conclusions or recommendations expressed in this material are those of the authors and do not necessarily reflect the views of the NSF, NIH, or NSERC.

Daniel.S.Esser@Vanderbilt.edu

dynamics of continuum robots (see e.g. [24], [38]–[40]), as well as provide a framework control [41].

Lagrangian methods for the modeling of continuum robots are another popular approach as they are well-suited to capture the dynamics and constraints of these systems. Typically when using a Lagrangian approach, the continuum structure is discretized, either as a constant-curvature segment [42] or as a series of discrete masses connected by elastic joints [43]; alternatively model basis functions to represent the strain field [44] have been suggested.

More general finite-element-based computational techniques (FEM) have been proposed to model the deformations of beams with spatially-varying mechanical properties [45]; this approach could, in theory, be integrated into a soft robot modeling framework such as SOFA [46]. While FEM can account for effects like cross sectional deformations, for many continuum robots (e.g. TDCRs) these effects are negligible. In this work we demonstrate that such tendon driven robots can be effectively modeled using a simpler system of ordinary differential equations rather than requiring a full volumetric model with partial differential equations. This has advantages in terms of computational efficiency, making it useful for design optimization and real-time control. The Cosserat rod equations can be numerically solved at multiple kilohertz with a standard computer, i.e. fast enough for real-time control, and to enable design optimization and planning [26], [47], [48].

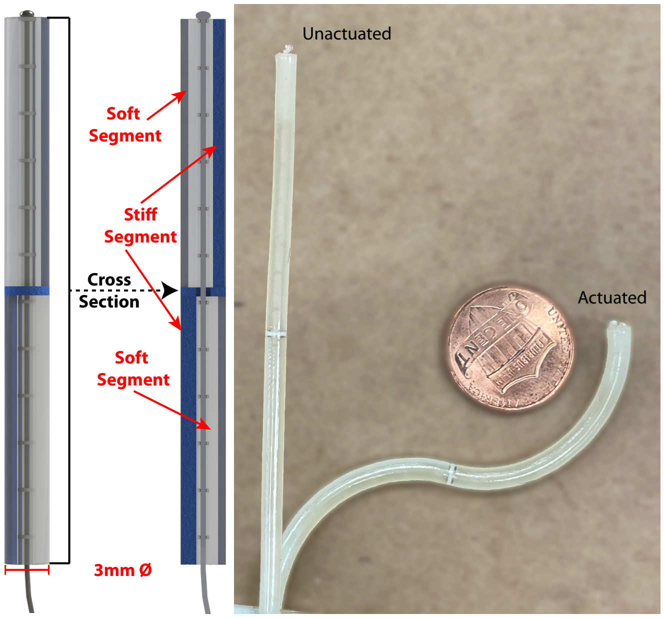

Fig. 1. An example of a continuum robot with an inhomogeneous stiffness profile and one straight tendon. Shifting the stiffness center along arclength enables the actuated curvature to dramatically change directions along arclength when actuated with a single straight-routed tendon.

In recent years, rapid prototyping techniques have advanced, enabling the fabrication of continuum robots with more general stiffness profiles, e.g. beyond traditional symmetric, homogeneous, and constant arclength cross-sections. Examples include concentric tube robots [49], [50], and pneumatic robots [31], [51], [52], among others. Various techniques enable straightforward creation of more complex general stiffness profiles along the arclength and across the cross section of the device, either using multimaterial printing [51], [53], or via selective material removal [54]–[56].

In this paper we show how projecting loads to the center of stiffness and treating it as the robot's backbone enables geometrically exact models for robots with (potentially) nonlinear tendons to apply exactly to multimaterial soft robots. This analogy enables a large body of prior work in Cosserat Rod modeling of such robots to be applied directly to those with stiffness variations. We also contribute experimental validation of this model using an additively manufactured, multimaterial tendon-actuated soft robot. We explore how the use of material variation to shift the stiffness center along the robot can be used to encode desired deformation profiles into a soft robot. These deformation profiles provide new tools for continuum robot designers to customize the behavior of their robots for a particular application. To illustrate the usefulness of this in an example application, we consider a neurosurgical procedure in which the surgeon must sweep the tool tip across a curved surface deep inside the brain. The goal is to touch as many points as possible on the surface with an electrosurgical probe, to reduce the size of the structure that creates cerebrospinal fluid. This can cure patients who suffer from hydrocephalus, i.e. over-production of this fluid, and hence have excessive pressure within their heads. We show how stiffness variation can improve performance of this task without increasing the complexity of the actuation system, by enabling the robot to deform into shapes that are more conducive to the constrained workspace.

MODELING APPROACH

Cosserat Rod Model

We base our rod modeling on standard assumptions: materials are linearly elastic, isotropic, and rods are slender, meaning cross-sectional deformations are negligible. These assumptions are generally reasonable for rod-like soft robots [24], [36], [57], but may not apply to fluidically driven soft robots, whose actuators can sometimes locally deform the material by 100% or more, or hydrostat-type actuators which leverage cross-sectional changes to elongate, bend, or contract. If materials with anisotropies are used (for example, fabric or string strain limiters are commonly used in soft robots), the constitutive stiffness law in the model would need to be reconsidered. We assume a common Poisson's ratio across a multimaterial robot's different Young's moduli. This assumption is reasonable for soft robots comprised of similar types of materials, but may not be the case if different classes of materials are combined (i.e. metals and elastomers).

The model proposed in this work is an extension of the coupled Cosserat rod and string model of [24], in which a robot with uniform stiffness and arbitrarily routed tendons was modeled. The model suggested in [24] consists of a set of ordinary differential equations for the position and orientation $\underline{p}$, $\boldsymbol{R}$, and internal forces and moments $\underline{n}, \underline{m}$ of the rod-like robot as they relate to the distributed applied forces and moments $\underline{f}$ and $\underline{l}$.

$$\begin{aligned} \dot{\underline{p}} &= \boldsymbol{R}\underline{v}, \\ \dot{\boldsymbol{R}} &= \boldsymbol{R}\hat{\underline{\omega}}, \\ \dot{\underline{n}} &= -\underline{f}, \\ \dot{\underline{m}} &= -\dot{\underline{p}} \times \underline{n} - \underline{l}, \end{aligned} \tag{1}$$

where $\hat{}$ is the skew operator. The forces and moments ($\underline{f}$ and $\underline{l}$) are the sum of the tendon loads and any external loads on the continuum robot.

The linear and angular rates of change of the rod reference frame are given by:

$$\begin{bmatrix} \underline{v} \\ \underline{\omega} \end{bmatrix} = \boldsymbol{K}^{-1} \begin{bmatrix} \boldsymbol{R}^T \underline{n} \\ \boldsymbol{R}^T \underline{m} \end{bmatrix} + \begin{bmatrix} \underline{v}^* \\ \underline{\omega}^* \end{bmatrix}. \tag{2}$$

Note that $\underline{v}^*$ and $\underline{\omega}^*$ describe the reference (unactuated) shape of the rod. In the case of a straight rod, these are $[0, 0, 1]^T$ and $[0, 0, 0]^T$ respectively. When the elastic member is chosen to be isotropic with a symmetric and homogeneous cross section and the reference frame is chosen to be at the center of the cross section and aligned with the principal axes, the stiffness matrix is diagonal, and is typically written in terms of its components:

$$\boldsymbol{K} = \begin{bmatrix} \boldsymbol{K}_{SE} & 0 \\ 0 & \boldsymbol{K}_{BT} \end{bmatrix},$$

where $\boldsymbol{K}_{SE} = diag(GA, GA, EA)$ and $\boldsymbol{K}_{BT} = diag(EI_{xx}, EI_{yy}, G(I_{xx} + I_{yy}))$. The cross sectional area A and the second moment of area I are geometric parameters in the stiffness matrices, while the Young's modulus E and the shear modulus $G = \frac{E}{2(1+\mu)}$ are material properties. The derivation of these matrices for the case of an inhomogeneous cross section is described in the subsequent section.

Elasticity of Inhomogeneous Cross Sections

First we consider the elastic properties of a general cross section. The axial stress, bending moments, torsional moment, and shear stresses can be written as:

$$n_z = v_z \int E\, dA + \omega_x \int Ey\, dA - \omega_y \int Ex\, dA. \tag{3}$$

$$m_x = v_z \int Ey\, dA + \omega_x \int Ey^2\, dA - \omega_y \int Exy\, dA, \tag{4}$$

$$m_y = -v_z \int Ex\, dA - \omega_x \int Exy\, dA + \omega_y \int Ex^2\, dA. \tag{5}$$

$$m_z = -v_x \int Gy\, dA + v_y \int Gx\, dA + \omega_z \int G(x^2 + y^2)\, dA. \tag{6}$$

$$n_x = v_x \int G\, dA - \omega_z \int Gy\, dA, \tag{7}$$

$$n_y = v_y \int G\, dA + \omega_z \int Gx\, dA. \tag{8}$$

Note that the Young's modulus $E = E(x, y, s)$ may vary within the cross section, and that the cross section need not be constant over arclength. Judicious choice of a reference frame can simplify these constitutive equations. If the origin of the coordinate system is chosen as the stiffness center, the sectional moments $\int Ex\, dA$ and $\int Ey\, dA$ are zero. Equivalently, the coordinates of the stiffness center are:

$$x_{nc} = \frac{\int Ex\, dA}{\int E\, dA}, \qquad y_{nc} = \frac{\int Ey\, dA}{\int E\, dA}. \tag{9}$$

Choosing the stiffness center $P_{nc} = \begin{bmatrix} x_{nc} & y_{nc} \end{bmatrix}^{\mathsf{T}}$ as the origin as shown in Fig. 2a, we have decoupled axial force and bending force. Further simplification can be achieved by choosing the coordinate system (x' and y') as the principal axes of the cross section so that:

$$\int Ex'y'\, dA = 0. \tag{10}$$

This is shown conceptually in Fig. 2a, where the stiffness center offset p_{nc} is calculated from equations 9 and the rotation R_{nc} from equation 10. In this case, equations 3 through 5 reduce to:

$$\begin{aligned} n'_z &= v_z \int E\, dA, \\ m'_x &= \omega_{x'} \int Ey'^2\, dA, \\ m'_y &= \omega_{y'} \int Ex'^2\, dA, \end{aligned} \tag{11}$$

where the quantities with $'$ are measured in a frame centered at the stiffness center and aligned with the principal axes.

We can apply a similar argument to decouple the shear and torsional modes of deformation. Assuming that any variation of the Poisson's ratio across the cross section can be neglected (resulting in $E \propto G$), the torsional and shear strains can be written as:

$$\begin{aligned} m'_z &= \omega_z \int G(x'^2 + y'^2)\, dA, \\ n'_x &= v_{x'} \int G\, dA, \\ n'_y &= v_{y'} \int G\, dA, \end{aligned} \tag{12}$$

Decoupling the modes of deformation by this choice of coordinate system simplifies the problem, since the bending stiffness matrix is now diagonal. The diagonalized bending stiffness matrices used in the Cosserat rod model can be computed by evaluating the integrals in (11) and (12).

At the stiffness center, the constitutive stress-strain law can be written as:

$$\begin{bmatrix} \underline{n}_{nc} \\ \underline{m}_{nc} \end{bmatrix} = \boldsymbol{K}_{nc}(\begin{bmatrix} \underline{u}_{nc} \\ \underline{v}_{nc} \end{bmatrix} - \begin{bmatrix} \underline{u}^*_{nc} \\ \underline{v}^*_{nc} \end{bmatrix}), \tag{13}$$

where the stiffness matrix at the stiffness center is:

$$\begin{aligned} \boldsymbol{K}_{nc} = diag(&\textstyle\int G\, dA, \int G\, dA, \int E\, dA, \\ &\textstyle\int Ex^2\, dA, \int Ey^2\, dA, \int G(x^2 + y^2)\, dA). \end{aligned} \tag{14}$$

The vector $\begin{bmatrix}\underline{u}^*_{nc} & \underline{v}^*_{nc}\end{bmatrix}^{\mathsf{T}}$ is referred to as the precurvature of the stiffness center path, shown in red in 2b. $\underline{u}^*_{nc}$ and $\underline{v}^*_{nc}$ are the differential forms of the translation and rotation described by p_{nc} and R_{nc} respectively. The curvature vector $\begin{bmatrix}\underline{u}_{nc} & \underline{v}_{nc}\end{bmatrix}^{\mathsf{T}}$ describes the deformed shape of the robot as a result of the applied loads. The path of the stiffness center can be thought of as analogous to a virtual homogeneous beam with precurvature. A homogeneous beam with symmetric stiffness has a diagonal stiffness matrix describing the elastic properties of the centerline of the beam. This means that, for example, when a normal force is applied to the center of the beam, it does not bend and only elongates/contracts. This is not the case with an asymmetric beam; a pure normal force at the centerline of the beam can cause bending. However we demonstrate that there exists a point (stiffness center) within the cross-section where the stiffness matrix is diagonal and a pure normal force does not cause bending. The path of the stiffness center along arclength is functionally equivalent to a homogeneous beam through that path, with the same stiffness matrix. The position of the stiffness center relative to each tendon defines the moment arm of the applied tendon force to the virtual homogeneous beam. By choosing stiffness parameters to route the stiffness center to a specific path relative to each tendon, one can change the direction and magnitude with which each tendon bends the soft robot.

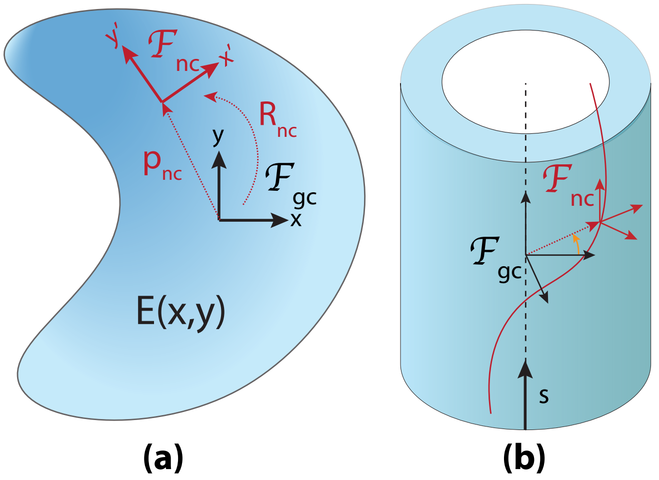

Fig. 2. (a) In a generic multimaterial cross section, the stiffness center frame (red) may be different from the geometric center frame (black). The stiffness center is offset by p_{nc}, with principal axes of the cross section rotated by R_{nc}. (b) The path of the stiffness center may vary nonlinearly along the arclength of the device. This path can be thought of as a virtual homogeneous and symmetric beam with precurvature.

APPLICATION TO A TWO-MATERIAL TENDON-OPERATED ROBOT

To demonstrate this modeling framework, consider an annular robot made of two materials, one stiffer than the other (Fig. 3). The wall of the device is fabricated with two materials with respective Young's moduli E_1 and E_2. θ_w is the angular width of the stiff portion of material, while θ_m is the angle of the midpoint of the stiffer segment (E_2) relative to the global coordinate system; this defines the axis of symmetry of the cross section. The stiffness center is guaranteed to lie on this axis of symmetry at a distance r_{nc} such that the moments of area relative to that point, weighted by the stiffness of the respective segments, are equal. With this choice, the radial and angular placement of the stiffness center can be parameterized by the two angles θ_w and θ_m.

The axis of symmetry shown in Fig. 3 is the principal axis of the inhomogeneous cross section. We assign a new frame corresponding to the stiffness center with an origin at the stiffness center and axes x_{nc} along the axis of symmetry, y_{nc} normal to x_{nc} and in the cross section plane, and z_{nc} parallel to the z axis of the geometric center frame z_{gc}, as shown in Fig. 2b. The homogeneous transformation from the geometric center to the stiffness center is

$$^{NC}\boldsymbol{T}_{GC} = \begin{bmatrix} \boldsymbol{R}_z(\theta_m(s)) & \underline{p}_{nc} \\ \boldsymbol{0}^T & 1 \end{bmatrix} \tag{15}$$

where,

$$\underline{p}_{nc} = \begin{bmatrix} r_{nc}(s)\cos(\theta_m(s)) \\ r_{nc}(s)\sin(\theta_m(s)) \\ 0 \end{bmatrix}. \tag{16}$$

is the offset of the stiffness center from the geometric center. With the relationship between the geometric center and the stiffness center known, we can thus express the reference twist of the stiffness center of the rod as,

$$\begin{aligned} \underline{v}^* &= \begin{bmatrix} 0 \\ 0 \\ \dot{\theta}_m \end{bmatrix} \\ \underline{\omega}^* &= \boldsymbol{R}^T \underline{\dot{p}}^*_{nc} \\ &= \boldsymbol{R}_z(\theta_m(s))^T \begin{bmatrix} \dot{r}_{nc}\cos\theta_m - \dot{\theta}_m \sin\theta_m \\ \dot{r}_{nc}\sin\theta_m + \dot{\theta}_m r_{nc}\cos\theta_m \\ 1 \end{bmatrix}, \end{aligned} \tag{17}$$

where $\dot{}$ denotes a derivative with respect to the arclength variable s, and * denotes the unactuated shape of the NC curve.

The cross section of the device is comprised of two annulus sectors with different Young's modulus values, as shown in Fig. 3. Given inner and outer radii r_i and r_o and spanning an angle of θ_d, the radius of the centroid from the center of the circle (which lies on the symmetric axis) of an annulus sector is

$$\bar{r} = \frac{4\sin\frac{\theta_d}{2}}{3\theta_d}\frac{r_o^3 - r_i^3}{r_o^2 - r_i^2}. \tag{18}$$

The radius of the stiffness center can be calculated as the centroid of each sector weighted by each respective area and Young's modulus:

$$\begin{aligned} r_{nc} &= \frac{\bar{r}_1 A_1 E_1 + \bar{r}_2 A_2 E_2}{A_1 E_1 + A_2 E_2} \\ &= \frac{4(r_o^3 - r_i^3)}{3(r_o^2 - r_i^2)}\frac{\sin(\frac{\theta_w}{2})}{\theta_w}\frac{E_1\theta_w - E_2(2\pi - \theta_w)}{E_1\theta_w + E_2(2\pi - \theta_w)} \end{aligned} \tag{19}$$

With the transformation between the geometric center and the stiffness center known, it is possible to calculate the

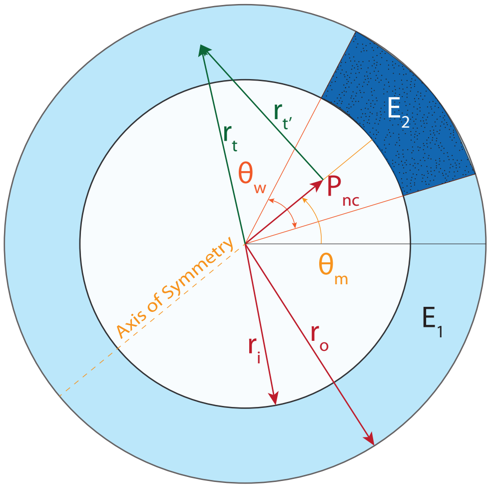

Fig. 3. A cross section of the two-material design parameterization used to vary the placement of the stiffness center as a function of arclength, where the dark blue denotes a stiffer material than the light blue.

moment of area of each segment of the cross section in the stiffness center frame:

$$
\begin{aligned}
I_{x_{nc}} &= \int_{(\theta_m-\theta_w/2)}^{(\theta_m+\theta_w/2)} \int_{r_i}^{r_o} (r\sin\theta)^2 r\, dr\, d\theta \\
I_{y_{nc}} &= \int_{(\theta_m-\theta_w/2)}^{(\theta_m+\theta_w/2)} \int_{r_i}^{r_o} (r\cos\theta - r_{nc}(s))^2 r\, dr\, d\theta.
\end{aligned}
\tag{20}
$$

With ${}^{NC}\boldsymbol{T}_{GC}$ known, we can now express the distributed forces and moments due to the tendons at the stiffness center and apply existing techniques to solve the Cosserat rod equations in the stiffness center frame, then convert the calculated deformations back to the geometric centerline of the device.

Effect of Stiffness Center Offset: Finite Element Demonstration

Previously, we described how an arbitrary cross section has a reference frame (the stiffness center) at which the stiffness matrix is diagonal. To demonstrate how this relates to the behavior of a simple asymmetric beam, we simulated a 20mm long segment of the constant offset prototype (parameters listed in Table I Constant N.C.) with a *Solidworks* (Dassault Systems) linear static finite element analysis. If a compressive load is applied to the cross section at the center of a homogeneous cross section, the beam would experience pure compression and no bending (disregarding buckling). However, in the case of an asymmetric cross section, when a compressive load is applied to the geometric center, it causes bending ($\theta_{tip} = 10.7°$ or $\kappa = 9.39\text{m}^{-1}$) because of the offset between the load and the stiffness center, as shown in the left of Fig. 4. The moment experienced at the stiffness center is the product of the force and the offset between the stiffness center and the point of load application.

We calculated the stiffness center offset using Eq. 19 and the cross sectional parameters in Table I; for this cross section the stiffness offset is $r_{nc} = 2.12\text{mm}$. Then, we applied the same load centered at the stiffness center of the cross section, as shown in the right of Fig. 4. The force is now a pure normal force in the stiffness center frame, and since the stiffness matrix is diagonal in this frame, the FEM simulation predicts pure compression (0.63mm or 3.2%) with negligible bending ($\theta_{tip} < 0.1°$). By modeling the robot in this reference frame, the deformation modes are decoupled, meaning that normal forces only cause compression/elongation, and moments only cause bending.

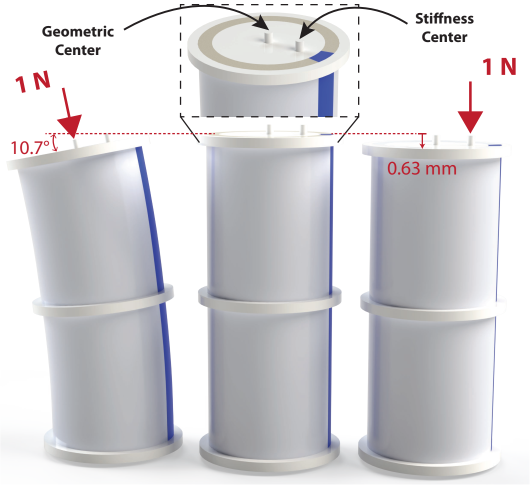

Fig. 4. Results of Finite Element Simulation of a 10mm segment of the constant offset stiffness center cross section. A small annular sector of the cross section is made of elastomer with a higher stiffness (shown in blue). On the left, a 0.5N normal load is applied at the geometric center which causes the prototype to bend to the left. On the right, the same load is applied to the stiffness center, which we calculated based on Equation 19. With the load at the stiffness center, the prototype experiences pure compression and no bending.

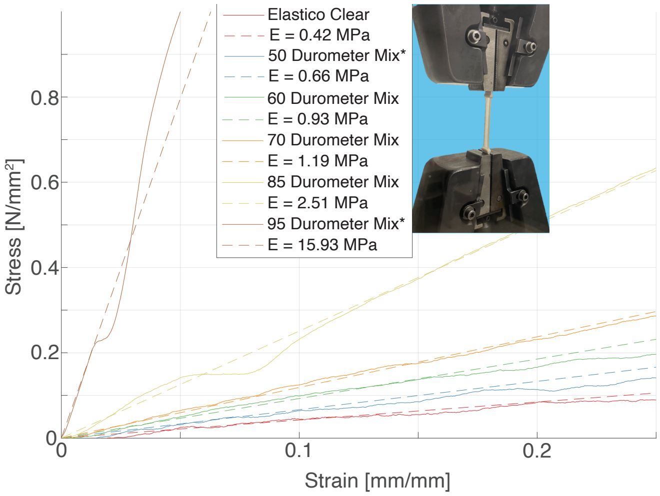

Fig. 5. Tensile testing of 3D printed samples with various mix ratios of elastic and rigid resin; * indicates materials that were used in the tendon manipulator prototypes.

PROTOTYPE FABRICATION AND EXPERIMENTS

We 3D printed our prototypes on a Multimaterial printer (*Stratasys: J35*). We used two materials to create asymmetric stiffness profiles: the 55D mix ratio and 95D mix ratio with Young's moduli of 0.66 and 15.93 MPa, respectively. These materials were chosen to demonstrate the effects of having materials with contrasting stiffness ($> 10\times$ difference in Young's modulus) in the robot cross-section. The manipulator features straight channels embedded in the elastic 3D printed structure to route the tendons. The tendon channels are threaded with 10 lb fishing line which is knotted and secured to the end of the device with cyanoacrylate glue.

We characterized the stiffness of a range of different material types available on the Stratasys J35 Polyjet printer with different stiffness achieved by mixing an elastic resin (Elastico FLX934) with a hard resin (VeroUltra White RGD825) during the printing process. The Young's modulus was determined by calculating the slope of the linear portion of each stress-strain curve. The stress-strain curves are shown in Fig. 5 alongside the linear fit used to determine the Young's modulus. As a point of reference, for a beam with radius 4mm and length 120mm bending in a 90° arc, the maximum strain is .05mm/mm; thus as Figure 5 shows, all of the materials remain relatively linear within this range.

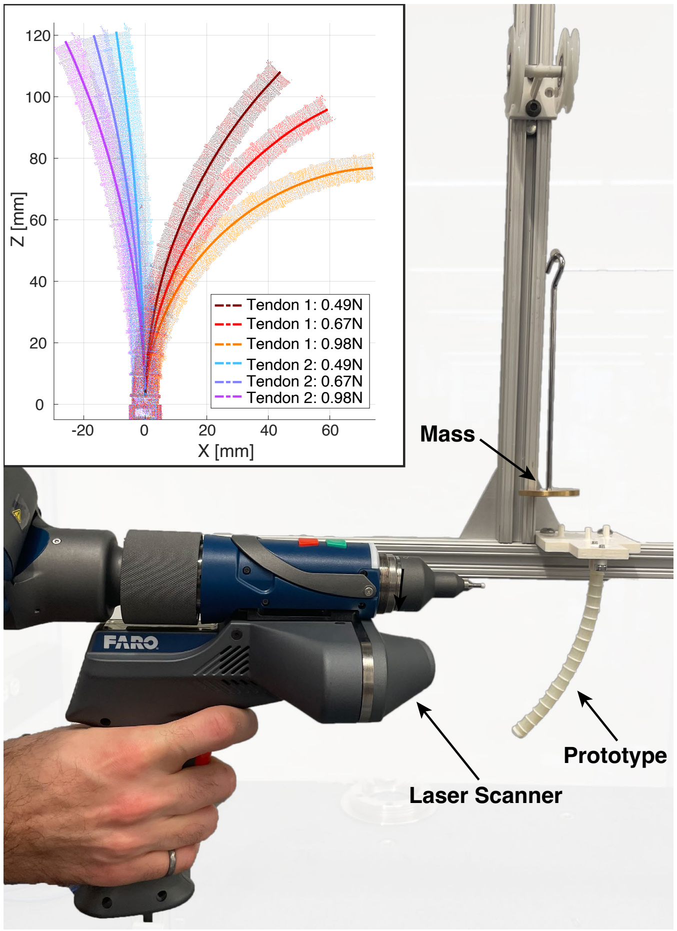

Fig. 6. Experimental setup to measure the robot shape. Inset: Point cloud data is converted to an arclength parameterized curve by sequentially fitting cylinders and interpolating with a spline.

TABLE I
PROTOTYPE DESIGN PARAMETERS

Prototype:	Constant N.C.	Helical N.C.
Outer Radius r_o	4mm	4mm
Inner Radius r_i	3.2mm	3.2mm
Length L	120mm	120mm
Position of Stiff Sector θ_m	π	$\pi{}^s/_L$
Width of Stiff Sector θ_w	$^\pi/_{16}$	$^\pi/_4 - (^\pi/_8)(^s/_L)$
Soft Material	50 Durometer Mix $E = 0.66\,\mathrm{MPa}$	
Stiff Material	95 Durometer Mix $E = 15.93\,\mathrm{MPa}$	
Tendon Locations	$\theta_{t1} = 0$, $\theta_{t2} = \pi$	$\theta_t = {}^\pi/_2$

To evaluate the proposed model on the prototypes, we measured their shape using a laser scanning coordinate measuring machine (*FARO Quantum Max Arm*). The setup used to measure the robot shape is shown in Fig. 6, and includes the laser scanner, the baseplate, and the robot. Some examples of pointcloud data and the measured rod shape are shown in the inset. In each experiment, we affixed a robot prototype to the rigid base with known features that we use to conduct a point-based registration of the base frame. We actuate the manipulator into several configurations with various calibration weights applied to the tendons. The shape of the geometric center of the rod is determined by sequentially fitting cylinders to the laser scanner point cloud in a piece-wise fashion using `lsqnonlin` in MATLAB.

The first prototype, called the constant offset stiffness center prototype, has a stiff section comprising 22.5° of the cross section, which did not change with arclength. This prototype demonstrates how offsetting the stiffness center can change the properties of the manipulator when actuated with tendons at different distances from the stiffness center. Both tendons are equidistant from the geometric center on either side, but the stiffness center is closer to one than the other, resulting in a different range of motion for each tendon. The second prototype, called the helically-varying stiffness center prototype, features a segment that varies helically along arclength while decreasing in width, showcasing the potential of moving the stiffness center to enable non-planar and non-constant curvature bending.

MODEL VALIDATION RESULTS

Constant Offset Stiffness Center Prototype

As mentioned earlier, the constant offset prototype has stiff material with a constant width and position in the cross section as a function of arclength, as described in Table I. As a result, the stiffness center is to the left (negative $\hat{x}$) of the geometric center, as shown in Fig. 7. Although both tendons are equidistant from the geometric center of the rod, the one at $\theta = 0$ has a larger moment arm from the stiffness center than the one at $\theta = \pi$. The two tendons were pulled at equal tensions, and the shape of the rod was measured using the laser scanning setup. The model-predicted (solid line) and measured (dashed line) shapes show the expected difference in bending between the two tendons. Table II

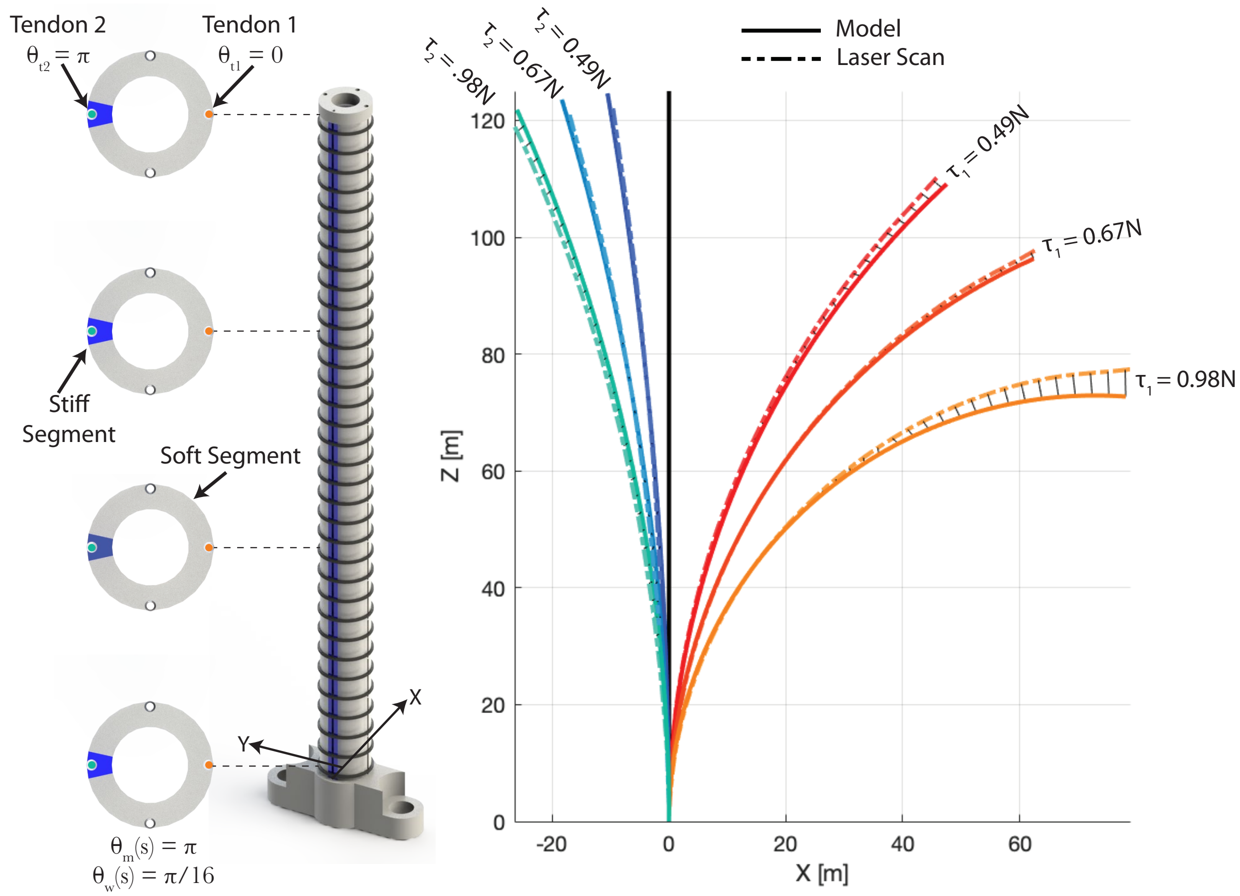

Fig. 7. Comparison of the model predicted backbone shape with laser-scanned backbone shape for the constant stiffness center prototype. The CAD rendering on the left shows the geometry of the soft tendon robot with a constant bi-material pattern in the cross-section. On the right, we show the model-predicted shape and the measured shape of the TDCR at these configurations. The offset stiffness center in this design effectively biases the workspace toward the other direction.

shows the numerical results for the tip error and shape error, which are all small relative to the sizes of the prototype. We note that the model prediction errors tend to increase with larger deformations both in absolute and percentage terms, as reflected in Table II. This may be a result of nonlinear material properties which become more prominent at higher strains. We also note that the model tends to over-predict curvature near the tip of the manipulator, compared to the experimental results - this is perhaps most apparent in the $\tau_1 = 0.98\text{N}$ case in Fig. 7. This is most likely a result of frictional losses causing a reduction of tendon tension over its arclength, which could, in future, be incorporated into the model to refine the accuracy. These results demonstrate how the workspace of a continuum robot can be biased in a particular direction through the use of multimaterial fabrication.

TABLE II
CONSTANT N.C. SUMMARY OF MODEL COMPARISON RESULTS

	Tendon Tension	Tip Error (% of L) $\|p(L) - \hat{p}(L)\|$	Shape Error $\int_{s=0}^{L} \frac{\|p(s)-\hat{p}(s)\|}{s}$
$\boldsymbol{\theta_{t1} = 0}$	$0.49N$	1.25 mm (1.0%)	1.6%
	$0.67N$	2.03 mm (1.7%)	2.3%
	$0.98N$	3.09 mm (2.6%)	2.8%
$\boldsymbol{\theta_{t2} = \pi}$	$0.49N$	1.37 mm (1.1%)	2.1%
	$0.67N$	1.99 mm (1.7%)	2.3%
	$0.98N$	3.97 mm (3.3%)	2.8%

Helical Offset Stiffness Center Prototype

The second prototype has an annular segment of stiff material with decreasing width and helically varying position in the cross section as a function of arclength. The design parameters of the cross section are shown in Table I. We tested a single straight tendon with an angular position of $\theta_t = \frac{\pi}{2}$. Since the stiffness center is not constant with respect to arclength in this prototype, the straight tendon applies a distributed moment, the direction of which changes along the robot. This causes the prototype to bend in a roughly helical shape, as shown in 8.

Note that near the middle of the manipulator, the curvature is the smallest because the tendon path is closer to the stiffness center, thus the magnitude of the moment is smaller, and as the tendon passes over the midpoint of the manipulator, the curvature switches directions. In Table III we show the computed tip and shape error. We note that in this more complex design, the shape error is slightly higher than the constant offset prototype, though the model generally predicts

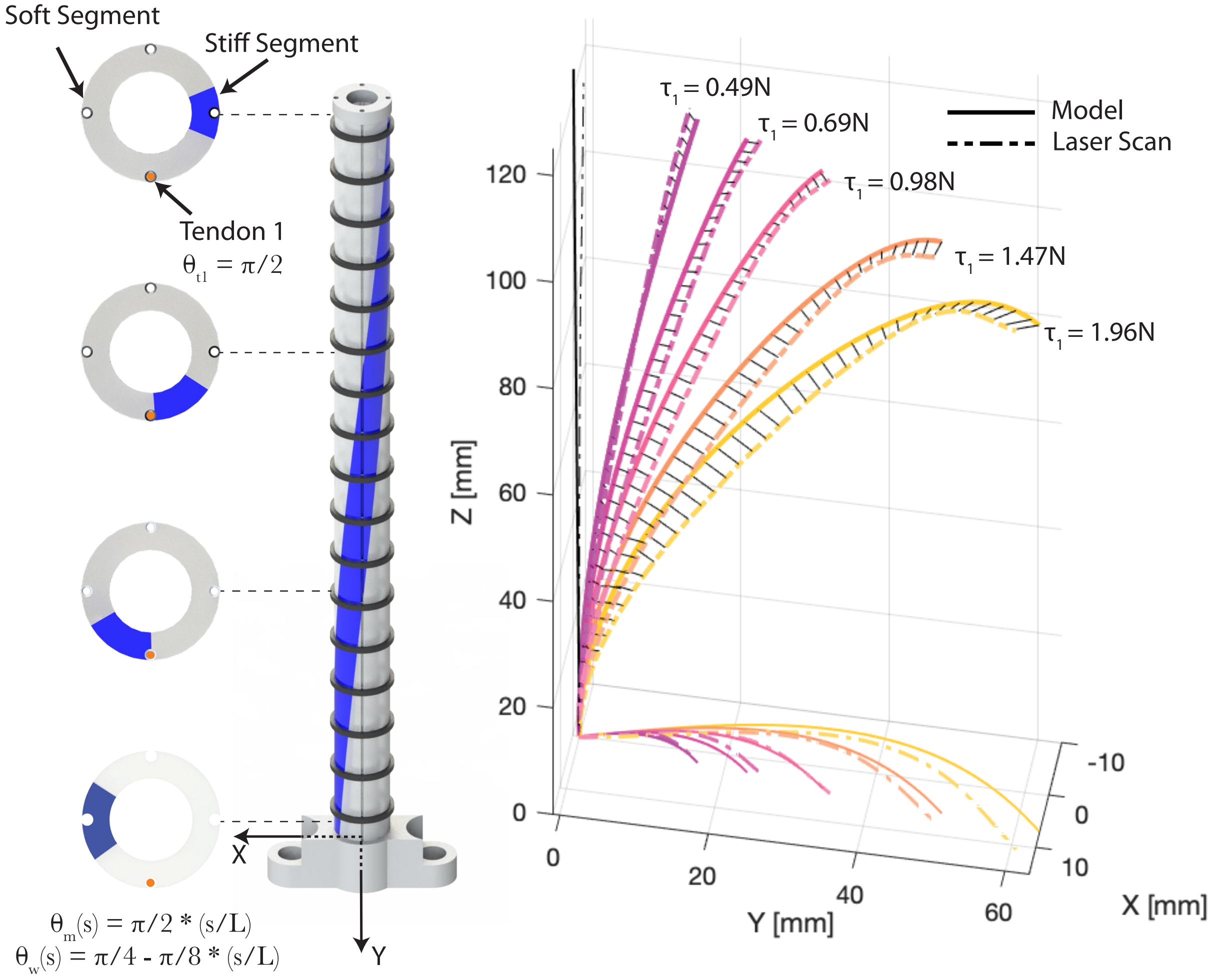

Fig. 8. Comparison of the model predicted backbone shape with laser-scanned backbone shape for the helical stiffness center prototype. The CAD rendering on the left shows the geometry of the soft tendon robot with a helically varying bi-material pattern in the cross-section, where the stiff segment becomes smaller towards the tip. On the right, we show the model-predicted shape and the measured shape of the TDCR at these configurations. With a straight tendon, pre curvature of the stiffness center causes the direction and magnitude of bending to change along arclength.

the correct deformed shape. The model-predicted curvature appears to change more smoothly along arclength, wherease the experimental results generally have high curvature near the base, become much straighter in the middle section, and then have higher curvature than the model at the top. These sharper changes in curvature in the experimental results appear to correspond to the points along arclength where the tendon crosses over the interface between the stiff and soft material. Its possible that there are local deformations at this interface layer that are not captured in the model, as a result of the abrupt local change in material properties. While we believe that the model is still reasonably accurate, local boundary layer interactions may be important to consider when designing soft robots with large variations in material stiffness (i.e. much greater than 10x difference in Young's Modulus).

EXAMPLE USE CASE: MORE CAPABLE NEUROSURGICAL TOOLS

Patients with hydrocephalus, a condition often affecting children, experience elevated pressure within their skulls due to an imbalance in the production and removal of cerebrospinal fluid. A potentially curative treatment involves cauterizing the surface of the choroid plexus, responsible for cerebrospinal fluid production [58]. Endoscopic Third Ventriculostomy (ETV) with Choroid Plexus Cauterization (CPC) has fewer re-operation rates compared to those who underwent ventriculoperitoneal shunt (VPS) placement [59]. Clinically today, the procedure is performed using a neuroendoscope which is introduced through the frontal cortex into the fluid-

TABLE III
HELICAL N.C. SUMMARY OF MODEL COMPARISON RESULTS

	Tendon **Tension**	**Tip Error (% of L)** $\|p(L) - \hat{p}(L)\|$	**Shape Error** $\int_{s=0}^{L} \frac{\|p(s)-\hat{p}(s)\|}{s}$
$\theta_t = \pi/2$	$0.49N$	1.47 mm (1.2%)	2.2%
	$0.69N$	2.85 mm (2.4%)	4.0%
	$0.98N$	3.15 mm (2.6%)	4.6%
	$1.47N$	3.47 mm (2.9%)	6.1%
	$1.96N$	1.69 mm (1.4%)	6.6%

filled ventricle [58]. These endoscopes have either rigid or flexible shafts, with tips that can bend in a constant-curvature arc (see Fig. 9b-c).

With existing neuroendoscopes, it can be challenging to cauterize the entire choroid plexus from the foramen of Monro to the posterior temporal horn [60]. A recent technical review concluded that success of the procedure is more likely with 90% cauterization coverage of the choroid plexus [61], however in another study showed the surgeon were only able to achieve the desired threshold of 90% coverage in 73% of CPC cases [62]. There is a clear clinical need for endoscopy tools that are designed so that their workspace can reach a greater percentage of the desired surface. With current tools there is a steep learning curve in mastering cauterization of the choroid plexus. Given variable patient anatomy, it can be very challenging to reach certain areas of choroid plexus, especially within the temporal horns.

Prior work toward robotic solutions for this procedure has explored use of concentric tube robots [63] and multi-tendon robotic device with nonlinear tendon routing [26], however both of these solutions are significantly more complex than existing single DOF manually-operated flexible endoscopes. We show below that a flexible endoscope with a more general stiffness profile can reach more of the choroid plexus surface than current clinical neuroendoscopes without the need for more complex, multi-DOF robotic actuation systems.

We compare a variable stiffness device (described below) with the clinical Karl Storz neuroendoscope, which is approved for use in third ventriculostomy and choroid plexus cauterization. It is 35 cm long, with an approximately 2 cm long actuated tip that has an angular range of motion from 0 to 270°. For the variable stiffness design, we consider a helically-varying stiffness center, using the same Young's modulus parameters for the bi-material cross section as the physical prototypes described in the prior sections. We placed the tendon at the geometric center of the prototype so that when actuated, the neuro-endoscope bends in a roughly helical shape. The ability to curve in a non-planar shape when actuated, using a single straight tendon, enables the device to better navigate around the structures of the brain to reach both sides of the choroid plexus. The specific design parameters used in this simulation are presented in Table IV.

To compare the two devices in terms of the kinematic reachability of the choroid plexus, we assume that both are introduced through a fixed entry vector into the frontal cortex to access the ventricle. We segmented the brain and ventricle from a preoperative MRI of a patient with hydrocephalus and annotated twenty desired cauterization points across the choroid plexus. This was performed by a surgeon experienced with hydrocephalus surgical interventions (co-author Naftel) to be clinically representative.

For both devices we consider that they can be inserted axially along the entry vector as desired and axially rotated about it as desired. The degrees of freedom (DOF) are shown in Fig. 9a as q_1, q_2, and q_3. The surgical approach and DOF for both the existing and proposed neuroendoscope are the same, except the tendon-actuated DOF q_3 bends the existing neuroendoscope into a constant curvature arc while the proposed design bends according to the model proposed in this paper.

TABLE IV
ARBITRARY STIFFNESS NEURO-ENDOSCOPE DESIGN PARAMETERS

Parameter	Value
Length of Actuated Tip	30cm
Width of Stiff Section θ_w	$\pi/2$
Angle of Stiff Section θ_m	$\pi - \pi s/L$
Young's Modulus of Soft Section E_1	0.66MPa
Young's Modulus of Stiff Section E_2	15.93MPa

To compare the performance of the two designs, we solved the inverse kinematics analytically for the constant curvature model of the Storz endoscope and numerically (using nonlinear least squares) for the arbitrary stiffness design. Reachable points are those where the endoscope tip was within 1mm of the desired position without penetrating the brain tissue (pink in Fig. 9).

The clinical endoscope was able to reach fourteen out of twenty points on the choroid plexus without collisions, mostly along the superior surface of the choroid plexus, which aligns with reports in medical literature [60]. In contrast, the arbitrary stiffness design reached eighteen of the twenty points. The non-planar actuated shape of the helical stiffness design enables the device to reach deeper towards the back of the workspace. The supplementary video demonstrates the results of the simulation, showing each endoscope navigating through its respective reachable set of points. Note that while each reachable point is collision-free, in the animation the motions between the points were linearly interpolated in joint space, in future it would be necessary to plan these motions in a collision-free manner. Note that the helical design was heuristically chosen to demonstrate how arclength-varying curvature achieved via material variation can enhance a continuum robot, in the future with design optimization of these parameters it might be possible to achieve better results.

This case study demonstrates how designs with general stiffness variation have the potential to improve the performance of clinical tools without requiring added actuation complexity, such as additional tendons or nonlinear tendon routing. We note that a variable stiffness endoscope like this could be fabricated using additive manufacturing (such as the method used in this paper) or using laser cutting (see e.g., [55]) to create desired asymmetric stiffness.

We believe that new rapid manufacturing approaches have great potential to revolutionize healthcare towards the development of specialized or modular devices where their properties can be tailored to a particular surgical application or even an individual patients anatomy. Rapid prototyping techniques are continually developing with new technologies that can be safely using in surgical applications. Vascular stents are commonly manufactured by lasercutting hyperelastic nitinol tubes [64], and this rapid fabrication technique is being used to build new types of continuum robots [56]. Biocompatible 3D printing workflows have also been developed (see e.g. Formlabs BioMed series) that may in future be used to manufacture

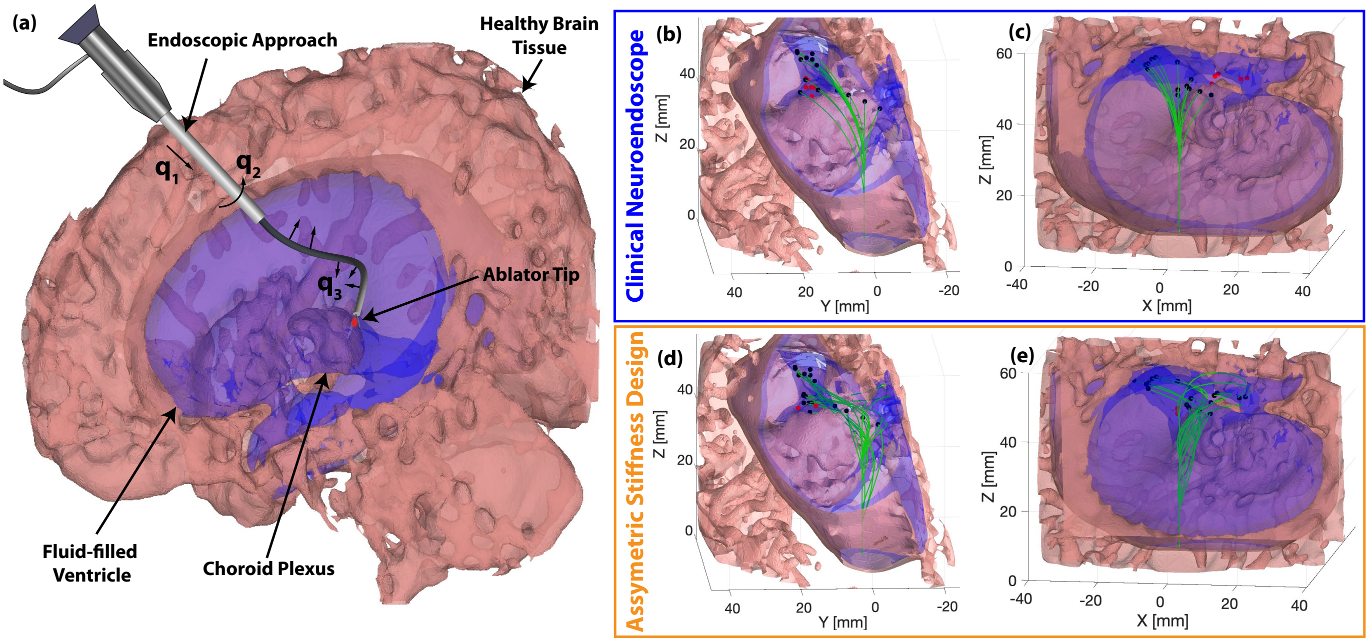

Fig. 9. Improving the navigability of a tendon-actuated flexible endoscope. (a) Conceptual image of a tendon-actuated endoscope with a helically varying stiffness profile over arclength. Two views of the workspace with the clinical endoscope (b, c) and the arclength-varying stiffness design (d, e). Reachable tip positions shown in black and associated backbone shape in green, unreachable points shown in red.

continuum robots with customized elastic properties. Silicone 3D printing is also being developed for medical applications [65], as silicone is known to be stable and biocompatible and commonly used in medical/cosmetic implants. While not the focus of this work, one key benefit of using stiffness profiles to design continuum robot motions, is that stiffness elements can be changed more easily than rerouting actuators. In the future, we envision continuum robot tools with, for example, hot-swappable sheaths with specific stiffness properties that can specialize the robot kinematics for a potential use case.

Once a functional prototype is developed, user testing will be conducted with neurosurgeons to ensure that they can comfortably navigate the device throughout its workspace to reach 90% coverage of the hippocampus. If needed, additional tendon-operated degrees of freedom could be added to this design to ensure that this goal is achievable across a range of patients. We note that deploying this in humans would require either an investigational device exemption or FDA clearance/approval, and are looking forward to securing an industry partner to construct this device under FDA-prescribed design controls and ultimately translate our results to the clinic.

Discussion and Conclusion

In this paper, we demonstrate how mapping forces to the stiffness center enables one to consider it as analogous to an arbitrarily shaped homogeneous backbone. This enables one to straightforwardly include stiffness variation across and along a soft manipulator within the existing Cosserat rod modeling framework. Using the stiffness center frame in the model provides an intuitive understanding of how changing the cross section affects the actuated shape of the manipulator. By arbitrarily routing the stiffness center along arclength relative to the location of actuation loads (tendons in our case), one can change both the magnitude and direction of bending of the soft arm. This has the effect of mechanically encoding the configurations of the soft robot to a desired non-planar shape even with simple, straight-routed tendons.

Overall, we showed that this modeling technique is capable of capturing the general shape of a multimaterial manipulator accurately. Of particular note is that no model calibration other than the stiffness measurements was required to match the model to experimental results.

Stiffness variation enables the design of soft robots with task-specific shapes and ranges of motion, without the need for complex actuation structures, such as nonlinear tendon routings or fluidic channels. The arrangement of material stiffness rather than tendon routing within a soft robot may be scalable to smaller robot designs, for example in continuum robotic microsurgical tools [66]. Future work could leverage this new design freedom to create manipulators with task-specific shape and stiffness profiles. We are particularly excited about the potential for asymmetric stiffness profiles in continuum robots that can be dynamically changed during the use of these robots. Various methods, from material phase change [67], [68], to frictional jamming techniques [69], [70]. For example, in our prior work, we proposed using geometrically patterned low melting point alloys to change directional stiffness properties in soft tendon-driven robots [71]. In this work, we validated the Cosserat rod model for passive stiffening structures, but note that there is an exciting opportunity to geometrically pattern more complex structures of active stiffening mechanisms to dynamically reconfigure the deformation modes during use of the soft robot.

As our neurosurgical example showed, stiffness variation can be a particularly important design parameter for small-diameter robots, in applications that place strong limits on the types of mechanisms, and number of actuators, that can be used. General stiffness profiles enabled by advances in additive manufacturing are a promising design tool to enable more customizable task-specific endoscope-like manipulators.

REFERENCES

[1] J. Burgner-Kahrs, D. C. Rucker, and H. Choset, "Continuum Robots for Medical Applications: A Survey," *IEEE transactions on robotics*, vol. 31, no. 6, pp. 1261–1280, 2015.

[2] D. R. Mangels, J. Giri, J. Hirshfeld, and R. L. Wilensky, "Robotic-assisted percutaneous coronary intervention," *Catheterization and cardiovascular interventions*, vol. 90, no. 6, pp. 948–955, 2017.

[3] F. Campisano, A. A. Remirez, C. A. Landewee, S. Calo, K. L. Obstein, R. J. Webster, and P. Valdastri, "Teleoperation and Contact Detection of a Waterjet-Actuated Soft Continuum Manipulator for Low-Cost Gastroscopy," *IEEE robotics and automation letters*, vol. 5, no. 4, pp. 6427–6434, 2020.

[4] S. Jiang, J. Lou, Z. Yang, J. Dai, and Y. Yu, "Design, analysis and control of a novel tendon-driven magnetic resonance–guided robotic system for minimally invasive breast surgery," *Proceedings of the Institution of Mechanical Engineers. Part H, Journal of engineering in medicine*, vol. 229, no. 9, pp. 652–669, 2015.

[5] Z. Yang, B. Zhao, L. Bo, X. Zhu, and K. Xu, "CurviPicker: a continuum robot for pick-and-place tasks," *Assembly automation*, vol. 39, no. 3, pp. 410–421, 2019.

[6] X. Dong, D. Axinte, D. Palmer, S. Cobos, M. Raffles, A. Rabani, and J. Kell, "Development of a slender continuum robotic system for on-wing inspection/repair of gas turbine engines," *Robotics and computer-integrated manufacturing*, vol. 44, pp. 218–229, 2017.

[7] Y. Zhang and G. Yan, "In-pipe inspection robot with active pipe-diameter adaptability and automatic tractive force adjusting," *Mechanism and machine theory*, vol. 42, no. 12, pp. 1618–1631, 2007.

[8] C. Abah, A. L. Orekhov, G. L. H. Johnston, and N. Simaan, "A Multi-Modal Sensor Array for Human-Robot Interaction and Confined Spaces Exploration Using Continuum Robots," *IEEE sensors journal*, vol. 22, no. 4, pp. 3585–3594, 2022.

[9] W. McMahan, V. Chitrakaran, M. Csencsits, D. Dawson, I. Walker, B. Jones, M. Pritts, D. Dienno, M. Grissom, and C. Rahn, "Field trials and testing of the OctArm continuum manipulator," in *Proceedings 2006 IEEE International Conference on Robotics and Automation, 2006. ICRA 2006*. IEEE, 2006, pp. 2336–2341.

[10] D. Jiang, Z. Cai, H. Peng, and Z. Wu, "Coordinated Control Based on Reinforcement Learning for Dual-Arm Continuum Manipulators in Space Capture Missions," *Journal of aerospace engineering*, vol. 34, no. 6, 2021.

[11] J. Yang, H. Peng, W. Zhou, and Z. Wu, "Integrated Control of Continuum-Manipulator Space Robots with Actuator Saturation and Disturbances," *Journal of guidance, control, and dynamics*, vol. 45, no. 12, pp. 2379–2388, 2022.

[12] S. Hirose and H. Yamada, "Snake-like robots [Tutorial]," *IEEE robotics & automation magazine*, vol. 16, no. 1, pp. 88–98, 2009.

[13] G. Chirikjian and J. Burdick, "Hyper-redundant robot mechanisms and their applications," in *Proceedings IROS '91:IEEE/RSJ International Workshop on Intelligent Robots and Systems '91*. IEEE, 1991, pp. 185–190.

[14] R. Buckingham, "Snake arm robots," *Industrial robot an international journal.*, vol. 29, no. 3, pp. 242–245, 2002.

[15] D. Trivedi, C. D. Rahn, W. M. Kier, and I. D. Walker, "Soft robotics: Biological inspiration, state of the art, and future research," *Applied bionics and biomechanics*, vol. 5, no. 3, pp. 99–117, 2008.

[16] B. A. Jones and I. D. Walker, "Kinematics for Multisection Continuum Robots," *IEEE Transactions on Robotics*, vol. 22, no. 1, pp. 43–57, 2006.

[17] N. Simaan, Kai Xu, Wei Wei, A. Kapoor, P. Kazanzides, R. Taylor, and P. Flint, "Design and Integration of a Telerobotic System for Minimally Invasive Surgery of the Throat," *The International journal of robotics research*, vol. 28, no. 9, pp. 1134–1153, 2009.

[18] R. Webster III, A. Okamura, and N. Cowan, "Toward Active Cannulas: Miniature Snake-Like Surgical Robots," in *2006 IEEE/RSJ International Conference on Intelligent Robots and Systems*. IEEE, 2006, pp. 2857–2863.

[19] P. Dupont, J. Lock, B. Itkowitz, and E. Butler, "Design and Control of Concentric-Tube Robots," *IEEE transactions on robotics*, vol. 26, no. 2, pp. 209–225, 2010.

[20] R. Cieślak and A. Morecki, "Elephant trunk type elastic manipulator - a tool for bulk and liquid materials transportation," *Robotica*, vol. 17, no. 1, pp. 11–16, 1999.

[21] D. Camarillo, C. Milne, C. Carlson, M. Zinn, and J. Salisbury, "Mechanics Modeling of Tendon-Driven Continuum Manipulators," *IEEE transactions on robotics*, vol. 24, no. 6, pp. 1262–1273, 2008.

[22] R. J. Webster III and B. A. Jones, "Design and Kinematic Modeling of Constant Curvature Continuum Robots: A Review," *The International Journal of Robotics Research*, vol. 29, no. 13, pp. 1661–1683, 2010.

[23] B. A. Jones, W. McMahan, and I. Walker, "Design and Analysis of a Novel Pneumatic Manipulator," *IFAC Proceedings Volumes*, vol. 37, no. 14, pp. 687–692, 2004.

[24] D. C. Rucker and R. J. Webster III, "Statics and dynamics of continuum robots with general tendon routing and external loading," *IEEE Transactions on Robotics*, vol. 27, no. 6, 2011.

[25] J. Starke, E. Amanov, M. T. Chikhaoui, and J. Burgner-Kahrs, "On the merits of helical tendon routing in continuum robots," in *2017 IEEE/RSJ International Conference on Intelligent Robots and Systems (IROS)*. IEEE, 2017, pp. 6470–6476.

[26] Margaret Rox, A. Copinga, R. Naftel, I. R. Webster, and A. Kuntz, "Optimizing Continuum Robot Tendon Routing for Minimally Invasive Brain Surgery," in *Hamlyn Symposium on Medical Robotics*, London, UK, 2022.

[27] R. Niiyama, D. Rus, and S. Kim, "Pouch Motors: Printable/inflatable soft actuators for robotics," in *Proceedings - IEEE International Conference on Robotics and Automation*. Institute of Electrical and Electronics Engineers Inc., 9 2014, pp. 6332–6337.

[28] A. A. Calderon, J. C. Ugalde, J. C. Zagal, and N. O. Perez-Arancibia, "Design, fabrication and control of a multi-material-multi-actuator soft robot inspired by burrowing worms," in *2016 IEEE International Conference on Robotics and Biomimetics, ROBIO 2016*. Institute of Electrical and Electronics Engineers Inc., 2016, pp. 31–38.

[29] A. Sedal, D. Bruder, J. Bishop-Moser, R. Vasudevan, and S. Kota, "A Continuum Model for Fiber-Reinforced Soft Robot Actuators," *Journal of mechanisms and robotics*, vol. 10, no. 2, 2018.

[30] J. Bishop-Moser and S. Kota, "Towards snake-like soft robots: Design of fluidic fiber-reinforced elastomeric helical manipulators," in *2013 IEEE/RSJ International Conference on Intelligent Robots and Systems*. IEEE, 2013, pp. 5021–5026.

[31] M. D. Gilbertson, G. McDonald, G. Korinek, J. D. Van de Ven, and T. M. Kowalewski, "Serially Actuated Locomotion for Soft Robots in Tube-Like Environments," *IEEE robotics and automation letters*, vol. 2, no. 2, pp. 1140–1147, 2017.

[32] X. Ke, J. Jang, Z. Chai, H. Yong, J. Zhu, H. Chen, C. F. Guo, H. Ding, and Z. Wu, "Stiffness Preprogrammable Soft Bending Pneumatic Actuators for High-Efficient, Conformal Operation," *Soft robotics*, vol. 9, no. 3, pp. 613–624, 2022.

[33] U. Yoo, Y. Liu, A. D. Deshpande, and F. Alamabeigi, "Analytical Design of a Pneumatic Elastomer Robot with Deterministically Adjusted Stiffness," *IEEE Robotics and Automation Letters*, vol. 6, no. 4, 2021.

[34] L. Wang, G. Del Giudice, and N. Simaan, "Simplified Kinematics of Continuum Robot Equilibrium Modulation via Moment Coupling Effects and Model Calibration," *Journal of Mechanisms and Robotics*, vol. 11, no. 5, 10 2019.

[35] J. Barrientos-Diez, M. Russo, X. Dong, D. Axinte, and J. Kell, "Asymmetric Continuum Robots," *IEEE robotics and automation letters*, vol. 8, no. 3, pp. 1279–1286, 2023.

[36] K. Oliver-Butler, J. A. Childs, A. Daniel, and D. C. Rucker, "Concentric Push-Pull Robots: Planar Modeling and Design," *IEEE transactions on robotics*, vol. 38, no. 2, pp. 1186–1200, 2022.

[37] J. A. Childs and C. Rucker, "A Kinetostatic Model for Concentric Push-Pull Robots," *IEEE transactions on robotics*, pp. 1–19, 2023.

[38] F. Renda, F. Boyer, J. Dias, and L. Seneviratne, "Discrete Cosserat Approach for Multisection Soft Manipulator Dynamics," *IEEE Transactions on Robotics*, vol. 34, no. 6, pp. 1518–1533, 12 2018.

[39] F. Boyer, V. Lebastard, F. Candelier, F. Renda, and M. Alamir, "Statics and Dynamics of Continuum Robots Based on Cosserat Rods and Optimal Control Theories," *IEEE transactions on robotics*, vol. 39, no. 2, pp. 1544–1562, 2023.

[40] H. Li, L. Xun, and G. Zheng, "Piecewise Linear Strain Cosserat Model for Soft Slender Manipulator," *IEEE transactions on robotics*, vol. 39, no. 3, pp. 1–18, 2023.

[41] A. A. Alqumsan, S. Khoo, and M. Norton, “Robust control of continuum robots using Cosserat rod theory,” *Mechanism and machine theory*, vol. 131, pp. 48–61, 2019.

[42] P. Pustina, C. D. Santina, F. Boyer, A. De Luca, and F. Renda, “Input Decoupling of Lagrangian Systems via Coordinate Transformation: General Characterization and its Application to Soft Robotics,” *IEEE transactions on robotics*, vol. 40, pp. 1–13, 2024.

[43] C. Rucker, E. J. Barth, J. Gaston, and J. C. Gallentine, “Task-Space Control of Continuum Robots using Underactuated Discrete Rod Models,” in *2022 IEEE/RSJ International Conference on Intelligent Robots and Systems (IROS)*. Piscataway: IEEE, 2022, pp. 10 967–10 974.

[44] F. Boyer, V. Lebastard, F. Candelier, and F. Renda, “Dynamics of Continuum and Soft Robots: A Strain Parameterization Based Approach,” *IEEE transactions on robotics*, vol. 37, no. 3, pp. 847–863, 2021.

[45] O. Weeger, S.-K. Yeung, and M. L. Dunn, “Fully isogeometric modeling and analysis of nonlinear 3D beams with spatially varying geometric and material parameters,” *Computer methods in applied mechanics and engineering*, vol. 342, pp. 95–115, 2018.

[46] P. Ferrentino, E. Roels, J. Brancart, S. Terryn, G. Van Assche, and B. Vanderborght, “Finite Element Analysis-Based Soft Robotic Modeling: Simulating a Soft Actuator in SOFA,” *IEEE robotics & automation magazine*, vol. 31, no. 3, pp. 97–105, 2024.

[47] J. Burgner-Kahrs, D. C. Rucker, H. B. Gilbert, P. J. Swaney, P. T. Russell, K. D. Weaver, and R. J. Webster, “A Telerobotic System for Transnasal Surgery,” *IEEE/ASME transactions on mechatronics*, vol. 19, no. 3, pp. 996–1006, 2014.

[48] C. Baykal, L. G. Torres, and R. Alterovitz, “Optimizing design parameters for sets of concentric tube robots using sampling-based motion planning,” *2015 IEEE/RSJ International Conference on Intelligent Robots and Systems (IROS)*, vol. 2015, pp. 4381–4387, 2015.

[49] K. Picho, B. Persons, J. F. D’almeida, N. E. Pacheco, C. Reynolds, and L. Fichera, “Multi Jet Fusion of Nylon-12: A Viable Method to 3D-print Concentric Tube Robots?” Tech. Rep.

[50] T. K. Morimoto and A. M. Okamura, “Design of 3-D Printed Concentric Tube Robots,” *IEEE transactions on robotics*, vol. 32, no. 6, pp. 1419–1430, 2016.

[51] Z. Wang, B. Zhang, W. Cui, and N. Zhou, “Freeform Fabrication of Pneumatic Soft Robots via Multi-Material Jointed Direct Ink Writing,” *Macromolecular materials and engineering*, vol. 307, no. 4, pp. 2 100 813–n/a, 2022.

[52] S. Dilibal, H. Sahin, J. O. Danquah, M. O. F. Emon, and J.-W. Choi, “Additively Manufactured Custom Soft Gripper with Embedded Soft Force Sensors for an Industrial Robot,” *International journal of precision engineering and manufacturing*, vol. 22, no. 4, pp. 709–718, 2021.

[53] Y. Zhang, C. J. Ng, Z. Chen, W. Zhang, S. Panjwani, K. Kowsari, H. Y. Yang, and Q. Ge, “Miniature Pneumatic Actuators for Soft Robots by High-Resolution Multimaterial 3D Printing,” *Advanced materials technologies*, vol. 4, no. 10, pp. 1 900 427–n/a, 2019.

[54] S. Park, J. Kim, C. Kim, K.-J. Cho, and G. Noh, “Design Optimization of Asymmetric Patterns for Variable Stiffness of Continuum Tubular Robots,” *IEEE transactions on industrial electronics (1982)*, vol. 69, no. 8, pp. 8190–8200, 2022.

[55] P. J. Swaney, P. A. York, H. B. Gilbert, J. Burgner-Kahrs, and R. J. Webster, “Design, Fabrication, and Testing of a Needle-Sized Wrist for Surgical Instruments,” *Journal of medical devices*, vol. 11, no. 1, pp. 0 145 011–0 145 019, 2017.

[56] K. Oliver-Butler, Z. H. Epps, and D. C. Rucker, “Concentric agonist-antagonist robots for minimally invasive surgeries,” in *SPIE Proceedings*, vol. 10135. SPIE, 2017, pp. 1 013 511–1 013 511.

[57] D. C. Rucker, “The mechanics of continuum robots: Model-based sensing and control,” *Ph.D thesis, Graduate school of Vanderbilt University*, vol. 3506877, 2011.

[58] A. Boaro, B. Mahadik, A. Petrillo, F. Siddi, S. Devi, S. Chawla, A. M. Abunimer, A. Feletti, A. Fiorindi, P. Longatti, F. Sala, T. R. Smith, and R. A. Mekary, “Efficacy and safety of flexible versus rigid endoscopic third ventriculostomy in pediatric and adult populations: a systematic review and meta-analysis,” *Neurosurgical review*, vol. 45, no. 1, pp. 199–216, 2022.

[59] B. C. Warf, D. S. Weber, E. L. Day, C. P. Riordan, S. J. Staffa, L. C. Baird, K. P. Fehnel, and S. S. D. Stone, “Endoscopic third ventriculostomy with choroid plexus cauterization: predictors of long-term success and comparison with shunt placement for primary treatment of infant hydrocephalus,” *Journal of neurosurgery. Pediatrics*, vol. 32, no. 2, pp. 201–13, 2023.

[60] A. G. Weil, A. Fallah, P. Chamiraju, J. Ragheb, and S. Bhatia, “Endoscopic third ventriculostomy and choroid plexus cauterization with a rigid neuroendoscope in infants with hydrocephalus,” *Journal of neurosurgery. Pediatrics*, vol. 17, no. 2, pp. 163–173, 2016.

[61] I. C. Coulter, M. C. Dewan, J. Tailor, G. M. Ibrahim, and A. V. Kulkarni, “Endoscopic third ventriculostomy and choroid plexus cauterization (ETV/CPC) for hydrocephalus of infancy: a technical review,” *Child’s nervous system*, vol. 37, no. 11, pp. 3509–3519, 2021.

[62] J. Riva-Cambrin, J. R. W. Kestle, C. J. Rozzelle, R. P. Naftel, J. S. Alvey, R. W. Reeder, R. Holubkov, S. R. Browd, D. D. Cochrane, D. D. Limbrick, C. N. Shannon, T. D. Simon, M. S. Tamber, J. C. Wellons, W. E. Whitehead, and A. V. Kulkarni, “Predictors of success for combined endoscopic third ventriculostomy and choroid plexus cauterization in a North American setting: a Hydrocephalus Clinical Research Network study,” *Journal of neurosurgery. Pediatrics*, vol. 24, no. 2, pp. 128–138, 2019.

[63] E. J. Butler, R. Hammond-Oakley, S. Chawarski, A. H. Gosline, P. Codd, T. Anor, J. R. Madsen, P. E. Dupont, and J. Lock, “Robotic Neuro-Endoscope with Concentric Tube Augmentation,” *Proceedings of the ... IEEE/RSJ International Conference on Intelligent Robots and Systems*, 2012.

[64] W. Jiang, W. Zhao, T. Zhou, L. Wang, and T. Qiu, “A Review on Manufacturing and Post-Processing Technology of Vascular Stents,” *Micromachines (Basel)*, vol. 13, no. 1, p. 140, 2022.

[65] M. M. Duran, G. Moro, Y. Zhang, and A. Islam, “3D printing of silicone and polyurethane elastomers for medical device application: A review,” *Advances in industrial and manufacturing engineering*, vol. 7, p. 100125, 2023.

[66] A. Leavitt, R. Lam, Nichols Crawford Taylor, D. S. Drew, and A. Kuntz, “Toward a Millimeter-Scale Tendon-Driven Continuum Wrist with Integrated Gripper for Microsurgical Applications,” in *Hamlyn Symposium on Medical Robotics*. Ithaca: Cornell University Library, arXiv.org, 2023.

[67] J. Zhang, R. H. Soon, Z. Wei, W. Hu, and M. Sitti, “Liquid Metal-Elastomer Composites with Dual-Energy Transmission Mode for Multifunctional Miniature Untethered Magnetic Robots,” *Advanced science*, vol. 9, no. 31, pp. 2 203 730–n/a, 2022.

[68] Z. Xing, F. Wang, Y. Ji, D. McCoul, X. Wang, and J. Zhao, “A Structure for Fast Stiffness-Variation and Omnidirectional-Steering Continuum Manipulator,” *IEEE robotics and automation letters*, vol. 6, no. 2, pp. 755–762, 2021.

[69] Y. Wei, Y. Chen, T. Ren, Q. Chen, C. Yan, Y. Yang, and Y. Li, “A Novel Variable Stiffness Robotic Gripper Based on Integrated Soft Actuating and Particle Jamming,” *Soft Robotics*, vol. 3, no. 3, pp. 134–143, 9 2016.

[70] B. Yang, R. Baines, D. Shah, S. Patiballa, E. Thomas, M. Venkadesan, and R. Kramer-Bottiglio, “Reprogrammable Soft Actuation and Shape-Shifting via Tensile Jamming,” *Sci. Adv*, vol. 7, 2021. [Online]. Available: https://www.science.org

[71] D. S. Esser, E. McCabe, T. E. Ertop, A. Kuntz, and R. J. Webster, “Directional Stiffness-Switching Soft Robots via Phase-Changing Metallic Spines,” in *2024 IEEE 7th International Conference on Soft Robotics (RoboSoft)*. IEEE, 2024, pp. 366–373.